The effects of gasification feedstock chemistries on the infiltration of slag into the porous high chromia refractory and their reaction products

Tetsuya Kenneth Kaneko [a,b], Jingxi Zhu [a,b,*], Nathan Howell [b], Peter Rozelle [c], Seetharaman Sridhar [d]

[a] US Department of Energy, National Energy Technology Laboratory, 626 Cochrans Mill Road, Pittsburgh, PA 15236, USA
[b] Department of Materials Science and Engineering, Carnegie Mellon University, 5000 Forbes Avenue, Pittsburgh, PA 15213, USA
[c] Office of Clean Energy Systems, US Department of Energy, FE-22/Germantown Building, 1000 Independence Ave. NW, Washington, DC 20585, USA
[d] International Digital Laboratory, University of Warwick, Coventry CV4 7AL, UK

HIGHLIGHTS

- Slags with compositions resembling ash derived from coal and petroleum coke were synthesized.
- Infiltration of synthetic slags was simulated with a thermal gradient induced in the refractory.
- The slag–refractory interactions under coal gasification conditions were investigated.
- The products of the slag–refractory interaction were examined and their formation was discussed.

ARTICLE INFO

ABSTRACT

Synthetic slags with compositions representative of carbonaceous feedstock derived from coal and petroleum coke were infiltrated into $90\%Cr_2O_3$–$10\%Al_2O_3$ refractory material with a temperature gradient induced along the penetration direction of the slag. Experiments were conducted with a hot-face temperature of 1723 K (1450 °C) in a CO/CO_2 gas mixture with a ratio of 1.8, which corresponded to an approximate oxygen partial pressure of 10^{-8} atm. Interactions between the slags and the refractory produced solid-solution spinel layers on the top interfaces of the refractory samples, whose chemistries reflected the compositions of major constituents of the starting slags. $FeCr_2O_4$ formed when samples were infiltrated with slag composition rich in FeO, which was typical for coals derived from eastern USA. $(Mg,Fe)Cr_2O_4$ formed when samples were infiltrated with slags, containing considerable concentrations of both MgO and FeO that were common in western US coals. In slags resulted from substituting 50% (by weight) of the coal feedstock by petcoke, similar solid solution phases formed as the pure coal counterparts, but with addition of V_2O_3, which originated from the petcoke feedstock. The chromium spinel layers, to a reasonable extent, limited infiltration by hindering the slag from flowing into the porous microstructure of the refractory and the formation mechanisms of the product layers were discussed. The $Fe(Cr,V)_2O_4$ layer that formed in the presence of petcoke ash exhibited an uneven morphology. As compared to the FeO rich slags, MgO rich slags penetrated further beyond the protective layers and into the refractory. Both of these phenomena could lead to increased refractory spallation rates in actual gasification conditions.

© 2013 Elsevier Ltd. All rights reserved.

1. Introduction

Entrained-flow gasification converts mixtures of carbon-based materials such as coal, biomass, and petroleum coke into synthesis gas (syngas), a fuel rich in carbon-monoxide and hydrogen gases. The flexibility to utilize a wide breadth of feedstock options can provide increased fuel flexibility and potentially greater reduction in CO_2 emissions when used with carbon capture and storage. However, with operation temperatures and pressures as high as 1600 °C and 2.8 MPa, the mineral impurities from the feedstock fuse together into slag, which attack the porous refractory lining that shields the external steel casing of the gasifier [1]. After slag infiltrates into the refractory, variations in the chemical and physical properties of the materials cause cracks and voids to form near the refractory surface to the point of penetration [2,3].

Penetration of molten slag into refractory is controlled by temperature, gasification atmosphere, refractory porosity, slag composition and interfacial surface properties of the slag with respect to microstructure and chemistry of the refractory material [4]. This

* Corresponding author at: Department of Materials Science and Engineering, Carnegie Mellon University, 5000 Forbes Avenue, Pittsburgh, PA 15213, USA. Tel.: +1 412 2685708; fax: +1 412 2687596.
   E-mail address: jingxiz@andrew.cmu.edu (J. Zhu).

analysis focuses upon understanding how slag composition influences the slag infiltration into porous refractory.

Petroleum coke (petcoke) is a carbonaceous by-product from petroleum processing. Petcoke has high energy value, high carbon content and lower impurity content than coal, and hence it has become an attractive alternative feedstock for gasifiers. As shown in the worldwide petcoke usage data in ref. [5], the increase is significant over the recent years and is projected to continue to grow. The total ash content of coal is typically around 10 wt%, whereas that of petcoke is 1–2 wt% [6]. However, one disadvantage with petcoke is its significant amount of vanadium oxides such that it may require the addition of additives such as limestone or silica sand to maintain required slag flow characteristics in the system. This can be further complicated where petcoke is used in a fuel blend, with coal. The compositions of the consequent slags depend on the source of petcoke and the coal that it is blended with. Some typical compositions of a few petcoke slags can be found in Ref. [7].

Vanadium has a number of valence states, which are strongly dependent on the temperature and oxygen partial pressure in the gasifier. However, the thermodynamic data and phase diagrams of VO_x in slag solutions are sparse in public databases [8], which render limited understanding of the thermo-physical properties such as change of slag viscosity and the mechanism by which vanadium-containing slags interact with refractory materials [7]. Although the trade may consider petcoke slags to possess similar behaviors to those of the coal slags [7], this has yet to be evaluated experimentally and extensively.

A number of refractory materials have been considered or evaluated for use with coal and petcoke feedstock in slagging gasifier environments, such as sintered or fused cast alumina-silicate, high alumina, chromia–alumina, chrome–magnesia, alumina, and magnesia, as well as SiC refractory materials [9–13]. Each of these refractory materials has its own merits and disadvantages in terms of corrosion and wearing. Alumina refractories are not used in slagging gasifiers with petcoke-containing feedstock because vanadium found in petcoke slags can aggressively attack alumina refractories, rapidly decreasing service life. Based on laboratory-scale tests and industry trials, chromia-containing refractories were found to have the best overall properties and performance to be used as hot-face refractory material, including refractories made with Cr_2O_3–Al_2O_3, Cr_2O_3–Al_2O_3–ZrO_2, and Cr_2O_3–MgO systems [13–15]. Therefore, this study only considered high chromia refractory, i.e. $90\%Cr_2O_3$–$10\%Al_2O_3$.

Representative slag chemistries were chosen and synthesized to simulate potential gasification feedstocks and their infiltration behaviors into $90\%Cr_2O_3$–$10\%Al_2O_3$ refractory were studied using microscopy and diffraction techniques to identify product phases and changes in morphology.

2. Materials and methods

2.1. Materials

Synthetic slags with compositions, resembling those created by the mineral impurities in representative feedstock for entrained-flow slagging gasifiers, were used in this investigation. Representative slag compositions [7,16] were selected by taking averages of ash constituents derived from petroleum coke (petcoke) and eastern and western coal feedstock from the United States, with the former having a more acidic ash composition and the latter being more basic. The slag compositions were determined for the feedstock blends: 100% eastern coal (EC), 50 wt% eastern coal – 50 wt% petcoke (ECP), 100% western coal (WC), and 50 wt% western coal – 50 wt% petcoke (WCP) feedstock. The ash contents of eastern coal, western coal and petcoke feedstocks are 10%, 9%, and 1%, respectively. The ECP and WCP slags are similar to their EC and WC counterparts, but contain minor additions of V_2O_3.

Oxide powders were weighed and mixed to their appropriate ratios, then pre-melted in a high-density Al_2O_3 crucible at 1500 °C for 2 h in a CO/CO_2 gas mixture with a ratio of 1.8 (corresponding to an oxygen partial pressure of approximately 10^{-8} atm) in order to ensure that the oxidation state of Fe and V ions were maintained constant. The slag was cooled at roughly 20 °C/min by lowering the sample and the surrounding Al_2O_3 furnace tube out of the hot-zone. The slag was then extracted from the crucible and ground into roughly 2 mm particles. The desired target compositions and the experimentally achieved compositions are summarized in Table 1.

Commercial $90\%Cr_2O_3$–$10\%Al_2O_3$ refractory bricks with fused grains were cored into cylindrical cups for accepting the slag. The outer dimensions of the samples were machined to a diameter of 5.08 cm and a height of 11.11 cm. The cup portions of the samples were machined to a diameter of 3.18 cm and a height of 3.49 cm. The composition of the refractory is summarized in Table 2.

3. Experimental methods

To verify the constituents and characteristics of the starting materials, the synthetic slags and the refractory in their virgin states were examined using an FEI Quanta 600 environmental scanning electron (ESEM) microscope with energy dispersive

Table 1
Target compositions and experimentally achieved compositions of synthetic slags. Experimental compositions were analyzed using XRF. Results are presented in oxide mol%.

	Slags	Al_2O_3	SiO_2	FeO	CaO	MgO	Na_2O	K_2O	V_2O_3	Basicity CaO/SiO_2
EC	Target	18.30	53.70	15.90	7.67	2.31	1.02	1.1		
	Pre-melted	19.07	53.08	15.19	7.79	2.13	0.82	1.90		0.15
ECP	Target	17.51	52.09	15.46	7.86	2.37	1.07	1.09	2.55	
	Pre-melted	17.15	51.13	14.91	9.04	2.50	0.90	1.71	2.66	0.18
WC	Target	10.48	32.50	9.42	29.30	11.45	6.12	0.74		
	Pre-melted	10.60	32.89	8.31	29.66	11.64	6.15	0.75		0.90
WCP	Target	10.18	32.14	9.44	28.19	11.00	5.76	0.77	2.52	
	Pre-melted	14.10	31.28	7.44	28.79	9.07	5.54	1.07	2.70	0.92

Table 2
Composition of $90\%Cr_2O_3$–$10\%Al_2O_3$ refractory. Results are presented in oxide mol%.

	Al_2O_3 (%)	SiO_2 (%)	Cr_2O_3 (%)	CaO (%)	MgO (%)	Fe_2O_3 (%)	Na_2O (%)
$90\%Cr_2O_3$–$10\%Al_2O_3$	9.87	0.05	89.65	0.21	0.13	0.09	0

spectroscopy (EDS), secondary-electron (SE), and back-scattered electron (BSE) imaging. The porosity and average pore size of the refractories were measured using a Micromeritic AutoPore IV 9500 Series mercury porosimeter. The starting slags and the refractory were pulverized and scanned using a P'analytical X-ray diffraction (XRD) system using a step size of 0.025° and an effective time per step of 2000 s. The viscosities of the synthetic slags were measured using a Theta Industries Inc. Rheotronic II, which employs the concentric cylinder method [17,18]. A spindle and crucible constructed from high-density Al_2O_3 and ZrO_2, respectively, were used. The experimental atmosphere consisted of a gas mixture of CO/CO_2 with a ratio of 1.8. Viscosity values were acquired isothermally in a step-cooling cycle from 1500 °C to 1300 °C at 25 °C intervals.

A vertical tube furnace, manufactured by Lindberg, was used to thermally treat the slag and refractory materials. The experimental setup is schematically shown in Fig. 1a. A temperature gradient was introduced along the penetration direction of the refractory cup by deliberately stepping the lower portions of the refractory cup below the hot-zone of the furnace. A COMSOL simulation was carried out with the refractory cup placed in position inside the furnace and applying the actual dimensions of the furnace setup, as displayed in Fig. 1b. This simulation provided a general view of the temperature distribution in the experimental setup. As projected by the simulation the lower portion of the refractory cup experienced lower temperatures than the hot face. The temperature gradient was designed to emphasize the native temperature gradients that exist in actual gasification reactors due to differential heating conditions at the hot-face and the cold-face of the refractory lining. Refractories in actual gasifiers can experience 100 K or greater drops in temperature at roughly 50 mm depths from the working hot-face.

The thermal profile along the slag penetration direction was experimentally measured. Holes were drilled into a dummy refractory cup bottom at a distance interval of 25.4 mm. The depth of each hole was about the radius of the refractory cup cylinder so that the thermocouple could be inserted to measure the temperature at the center of the cylinder, not just the surface. The temperatures measured from the cup bottom are shown in Fig. 2 and confirms the successful introduction of a temperature gradient. In the actual infiltration experiments, once the desired thermal
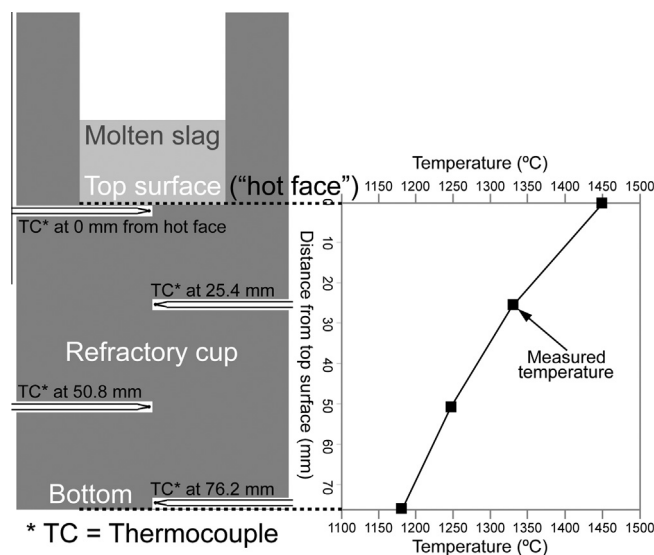

Fig. 2. Schematic drawing of measuring the temperature gradient on the refractory cup along the infiltration direction of the slag and the experimentally measured temperature profile.

profile was achieved, 40 g of granulated slag was inserted into the top of the furnace through a quartz tube. An illustration of the deposition process is shown in Fig. 1. The experiments were conducted in the same CO/CO_2 atmosphere used for melting the slag. The objective of the experiments was to simulate conditions similar to those encountered in entrained-flow gasifiers, which typically operate at oxygen partial pressures between 10^{-9} atm and 10^{-7} atm. The slag was deposited onto the refractory at temperature rather than placed there before the heating cycle to ensure that slag would not infiltrate into the refractory before the proper experimental conditions were met. The furnace was immediately re-sealed after the deposition. After an isothermal holding of 5 h, the refractory sample was cooled at roughly 15 °C/min and lowered out of the hot zone of the furnace. The sample was not rapidly quenched to room temperature because that could induce micro-cracks and damage the microstructures of the samples.
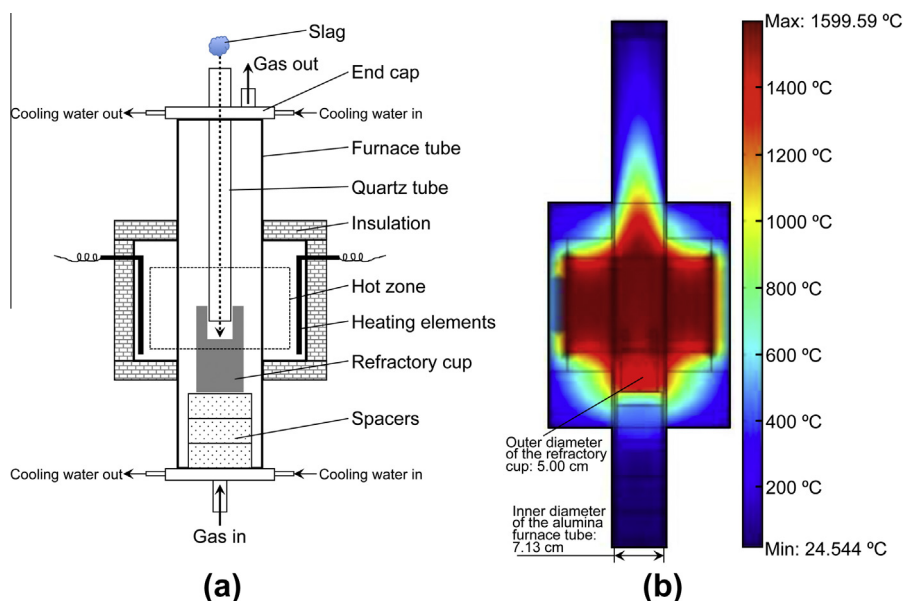

Fig. 1. (a) Illustration of the experimental setup and the deposition process of the slag onto the refractory sample (not drawn to scale); (b) graphical representation of the projected temperature gradient in the furnace modeled using COMSOL (drawn to scale).

The refractory cups containing slags were cross-sectioned to expose the slag infiltration into the refractory and progressively polished to a 0.5 μm using diamond suspensions. Polished samples were examined using the ESEM for morphological observations and chemical analyses. Portions of the samples were pulverized and analyzed using XRD to examine the crystalline phases.

4. Results

4.1. Characterization of Starting Materials

XRD powder scans of the pre-melted slag materials in Fig. 3 demonstrated that crystalline phases formed in the ECP, WC, and WCP slags. The ECP slag contained a solid solution $Fe(Al,V)_2O_4$ spinel phase that presented substantial peak broadening due to variations in composition. The WC slag contained spinel ($MgAl_2O_4$), akermanite ($Ca_2MgSi_2O_7$), merwinite ($Ca_3MgSi_2O_8$), and nephelite ($(K,Na)AlSiO_4$). The WCP slag contained similar crystalline phases including spinel, akermanite, merwinite, nephelite, and jadeite ($NaAlSi_2O_6$). EDS analysis showed that some of the phases containing Al_2O_3 in the WCP slag also consisted of varying concentrations of V_2O_3. The viscosity measurements of the starting slags with respect to temperature are displayed in Fig. 4. EC slag was glassy and exhibited Newtonian behavior. Little crystalline solids were found in post-viscosity measurement examination of EC slag. The other 3 slags all showed non-Newtonian flow behavior below ∼1723 K (1450 °C) and their viscosities were plastic due to significant

amount of crystalline solids present in the slags during viscosity measurement, which was confirmed by examine the post-measurement slags and also by separate quenching experiments. From an operations standpoint, Fig. 4 shows that the coal/pectcoke blends can be expected to produce slags that will differ in flow characteristics from slag produced by their pure coal counterparts.

The porosity of the refractory material was characterized, and the plot in Fig. 5 demonstrates that two distinct pore distributions were present. The larger pores, which constituted the majority of the porosity, corresponded to the pores constructed by the microstructure of the fine Cr_2O_3–Al_2O_3 particles in the matrix region. The smaller pores corresponded to the porosity within the fused Cr_2O_3–Al_2O_3 aggregates and particulates. The refractory bricks exhibited a porosity of 11.23% and mean pore radius of 1.47 μm.

The refractory material comprised of two structurally distinct regions, as illustrated in Fig. 6a. Dispersed throughout the refractory were densely packed, fused aggregates with low porosity. The BSE micrograph of the 90%Cr_2O_3–10%Al_2O_3 system illustrates that variations in composition of the aggregates were present. The brightly contrasted regions contained higher concentrations of Cr_2O_3 while the darkly contrasted regions contained higher concentrations of Al_2O_3. The regions surrounding the aggregates were the matrix, where finer particles sintered together and packed between the larger aggregates. The glassy alumino-silicate bond system designed to assist in the bonding behavior is shown in Fig. 6b. Prior studies observed that areas of refractory damage due to interactions with slags were focused in the porous matrix regions [19,20]. The XRD scan of the refractory in Fig. 7 displays peaks
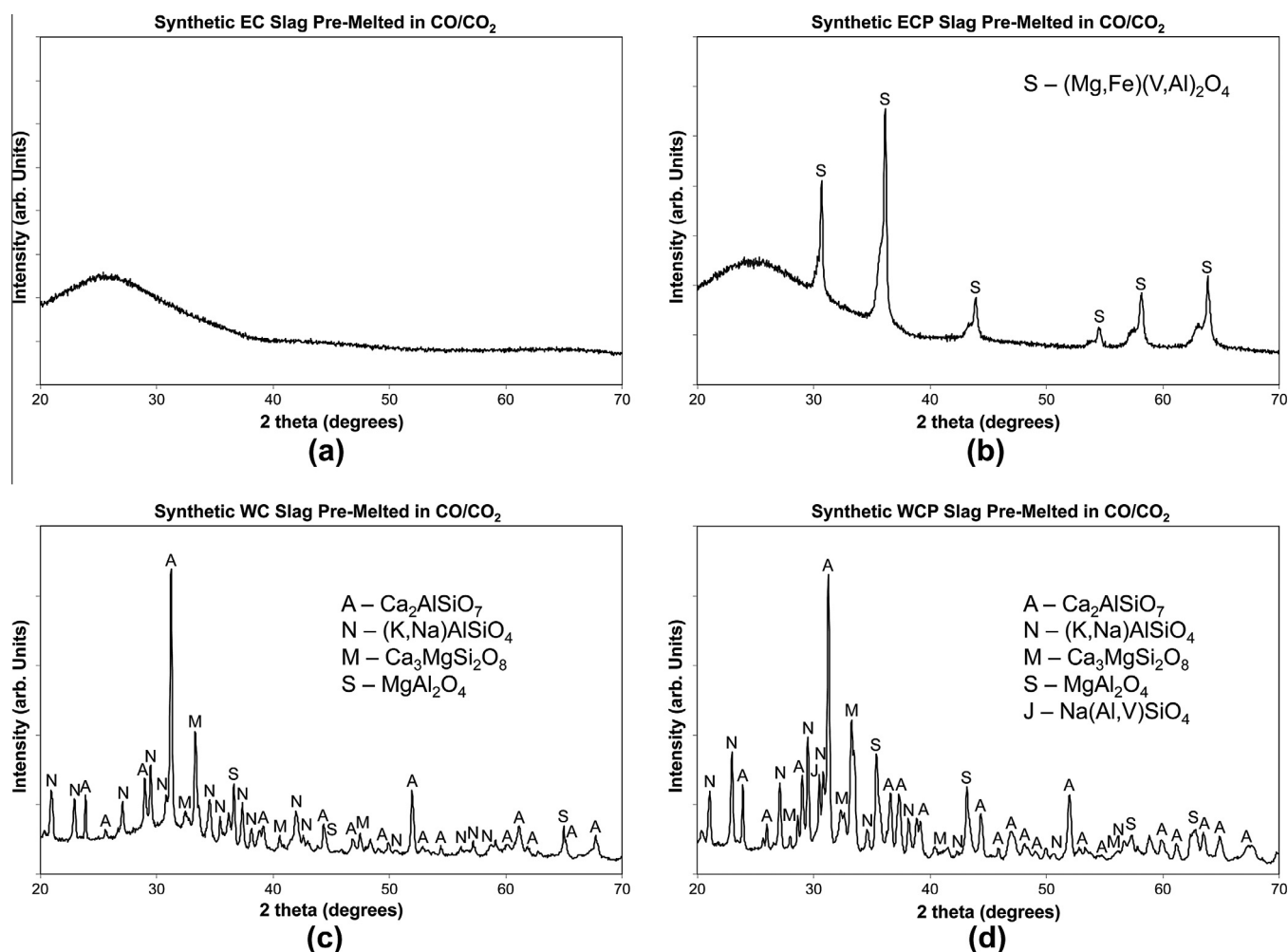

Fig. 3. XRD powder scans of starting synthetic (a) EC, (b) ECP, (c) WC, and (d) WCP slags melted in CO/CO$_2$ atmosphere.
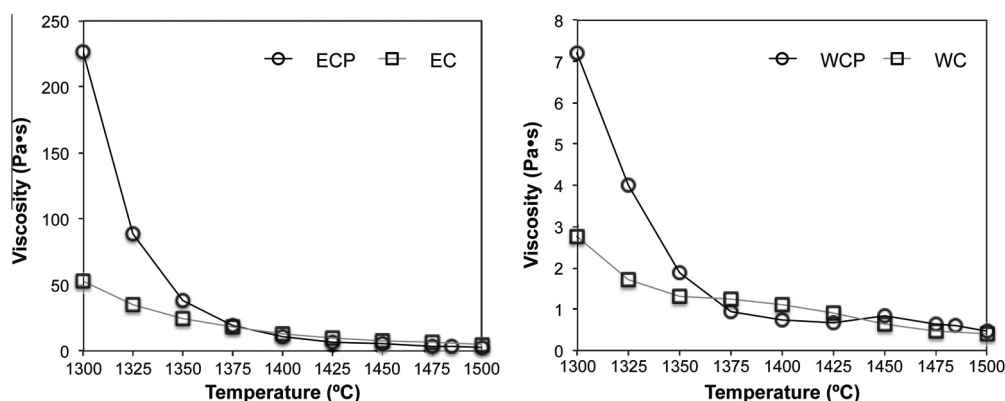
Fig. 4. Viscosity measurements of the starting EC, ECP, WC and WCP slags with respect to temperature.
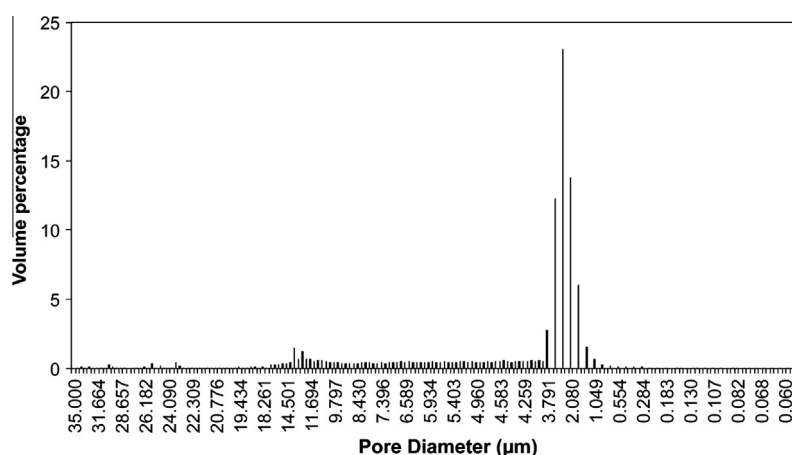

Fig. 5. Pore size distribution of 90%Cr_2O_3–10%Al_2O_3 refractory. The mean pore radius was 1.47 μm. The plot demonstrates that the refractory microstructure constructed two well-defined pore size distributions.
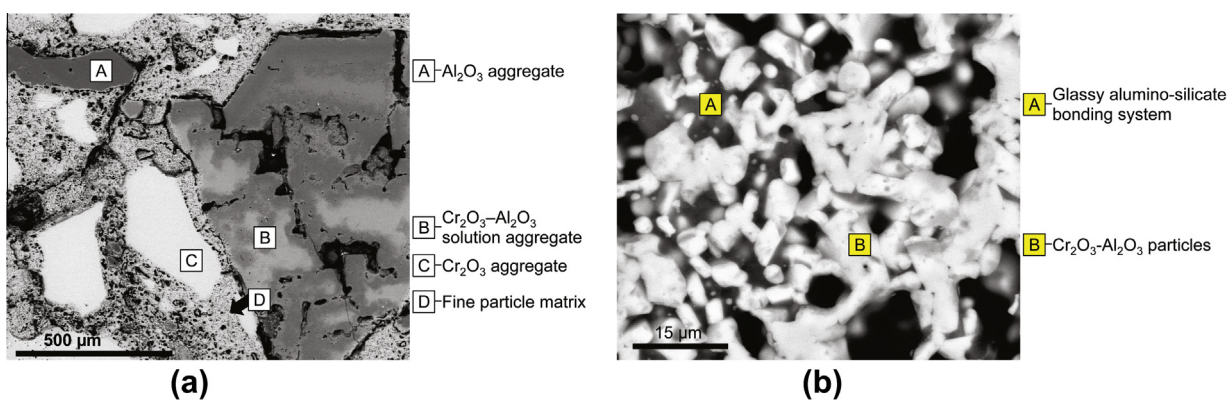

Fig. 6. BSE micrograph of (a) an un-infiltrated region of the Cr_2O_3–Al_2O_3 refractory, in which two distinct microstructures were evident and (b) the matrix region of Cr_2O_3–Al_2O_3 refractory.

attributable to a solid solution Cr_2O_3–Al_2O_3 phase with different lattice parameters.

4.2. Macroscopic infiltration trends

Photographs of the cross-sectioned infiltrated refractory samples are shown in Fig. 8. The photos were acquired with strictly the same lighting and camera parameters. Because of the dark green shade of the high-chromia refractory material, the output levels of the histograms of the original photos were adjusted to

the same parameters so as to reveal the contrast between infiltrated and un-infiltrated refractory materials. Beneath the top interface, infiltrated refractory material appeared in a darker contrast comparing to un-infiltrated refractory. The areas of infiltrated refractory were indicated in Fig. 8. Macroscopically, the infiltration depth of EC slag seemed slightly deeper than that of ECP slag while the depths for WC and WCP slags were comparable. The infiltration on the EC sample seemed non-uniform, i.e. the infiltration on the right-hand side was more severe than the left-hand side. Subsequent SEM examination revealed that this was caused by a small
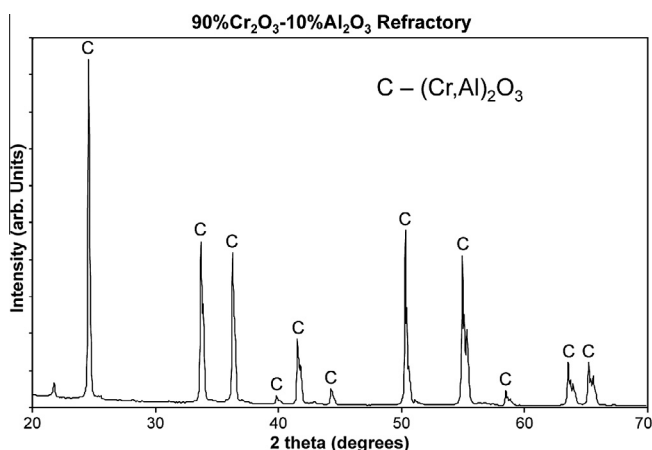
Fig. 7. XRD powder scan of 90%Cr_2O_3–10%Al_2O_3 refractory material before infiltration. The refractory consists of solid solution Cr_2O_3–Al_2O_3.

coincidental cluster of relatively large pores. Also, it was evident that WC and WCP slags penetrated much deeper into the refractory compared to EC and ECP slags. A very rough estimation of the infiltration depths from EC, ECP, WC and WCP slags were approximately 2.5, 1.5, 7.5 and 7 mm, respectively. The slag that did not infiltrate into the refractory pooled and formed a vitreous phase on the top interfaces of the samples during cooling. The infiltration depth difference was also reflected by the amount of slags left in the reservoir, given that the same initial amounts of slag were deposited into the refractory cups.

4.3. Slag infiltration and reaction

BSE micrographs of the top interfaces of the refractory infiltrated with the four slags, with accompanying EDS elemental maps, are shown in Figs. 9–12. While a product phase formed on the slag/refractory interfaces of the Cr_2O_3–Al_2O_3 refractory in all four cases, the product phases demonstrated different thicknesses and solution chemistries depending on the compositions of the starting slags. Table 3 summarizes these variations. The product layer resulted from ECP slag was much thicker than that resulted from EC, WC and WCP slags. This particular product layer also showed an uneven morphology that protruded into the slag. XRD scans of the top interface regions confirmed the presence of solid solution spinel phases and the solid solution Cr_2O_3–Al_2O_3 phase of the refractory, shown in Fig. 13. The akermanite and nephelite peaks originated from the edges of the refractory, where portions of the slag reservoir remained attached. The peak positions and relative intensities of the XRD scans of the slag reservoirs resolved the same phases as those observed in the starting slags that are displayed in Fig. 3. Also, for WC and WCP slags, granular crystals were seen suspended in the slag above the product layer. The grains were identified as solid solution spinel phases with Al_2O_3 and V_2O_3 substituting for Cr_2O_3. Since the refractory cups were not quenched, there would be crystals precipitating during cooling. It is believed that the dendrites seen in the ECP slag formed during of cooling (Fig. 10). For WC and WCP slag, it was not as clear whether the suspended crystal right above the product layer formed before or during cooling. Crystals of similar morphology was also seen in separately quenched slags. Therefore, while the possibility that these suspended crystals formed during cooling could not be ruled out, it was equally likely that they formed during the isothermal holding.

Besides the different thickness and morphological in the product layers resulted from the four slags, there were some other noticeable differences among the slags. On the sample infiltrated with EC slag, Fig. 9, the product layer comprised of two regions with different elemental distributions. The region adjacent to the slag reservoir was slightly enriched in Fe and Al comparing to the region adjacent to the Cr_2O_3 aggregate. Fig. 14a shows the
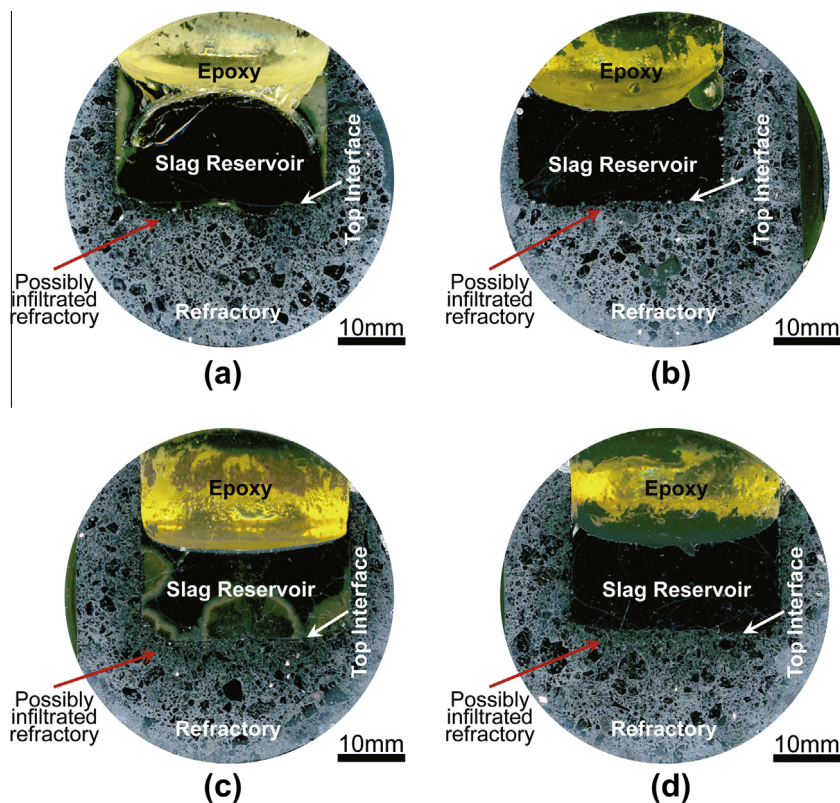

Fig. 8. Photographs of 90%Cr_2O_3–10%Al_2O_3 refractory sample infiltrated with (a) EC, (b) ECP, (c) WC and (d) WCP slag. The penetration was macroscopically visible.

Table 3
Average solid solution chemistries and thicknesses of the product layers.

	Solid solution chemistry	Surface morphology	Thickness (μm)
EC	$(Fe_{0.91}Mg_{0.09})(Cr_{0.81}Al_{0.19})_2O_4$	Smooth	55.1
ECP	$Fe(Cr_{0.42}V_{0.29}Al_{0.29})_2O_4$	Rough	98.2
WC	$(Mg_{0.67}Fe_{0.33})Cr_2O_4$	Smooth	44.7
WCP	$(Mg_{0.67}Fe_{0.33})Cr_2O_4$	Smooth	44.6

elemental profiles across the product layer, in which a spike in Al profile can be seen at the slag/product layer interface. This was in agreement of the findings in ref. [7], which suggested that the phases in the slag/refractory boundary area were in the sequence of slag, $FeAl_2O_4$ (hercynite), $FeCr_2O_4$ (chromite) and Cr_2O_3 refractory aggregate. The BSE micrograph in Fig. 14a showed that the boundary between $FeAl_2O_4$-rich and $FeCr_2O_4$-rich spinels was not abrupt; rather, there was a concentration gradient of decreasing Al content across a small distance toward the interior of Cr_2O_3 aggregate. A small amount of Mg^{2+} solutioned into the spinel layer as well. The average composition of $FeCr_2O_4$-rich spinel was approximately $(Fe_{0.91}Mg_{0.09})(Cr_{0.81}Al_{0.19})_2O_4$. The surface of $FeAl_2O_4$-rich layer appeared to be slightly jagged and rough.

The spinel layer on the top interface resulted from ECP slag, Fig. 10, showed no abrupt boundary within the product layer, but a gradual change in the composition across the thickness direction. The elemental profiles of V and Cr and the elemental profiles displayed in Fig. 14b shows the concentration gradient across the product layer. While the Cr concentration decreased from the chromia aggregate toward the slag, V concentration decreased in the opposite direction. A spike in Al profile can also be seen in Fig. 14b, similar to but smaller than the one in the EC slag case. The overall average composition of the product layer was $Fe(Cr_{0.42}V_{0.29}Al_{0.29})_2O_4$. Micro-cracks were occasionally seen at the boundary between the product layer and the refractory aggregates.

In the WC slag case, see Fig. 14c, both Fe and Mg showed a relatively constant concentration in the product layer and a steep drop a few micro-meters away from the spinel/refractory interface. Very small amount of Al entered the solid-solution spinel phase. In contrast, neither Al nor V participited in the formation of product layer of WCP slag comparing to ECP slag, which is evident in Fig. 14d. Both elements appeared to enrich in the suspended crystals instead.

The Fe map in Fig. 9, the V map in Fig. 10, the Ca maps in Figs. 11 and 12 also illustrate that slags infiltrated into the refractory, as previously seen macroscopically in Fig. 8. For instance, the Ca maps in Figs. 11 and 12, which is associated with the slag due to its high concentration of CaO, demonstrates that variable volumes of slag passed through the spinel layers and penetrated into the bulk refractory. WC and WCP slags penetrated deeper into the refractory as compared to the EC and ECP slags.

EDS point analyses from pockets of infiltrated slag were averaged to produce the compositions of the infiltrated slags shown in Table 4. As a reasonable approximation, it has been shown in ref. [19] that the slag composition virtually did not change after infiltration. In all four cases, SiO_2 content in the penetrated slags increased significantly, as determined by mass-balanced comparison of the compositions listed in Tables 1 and 4. There was some CaO enrichment for both WC and WCP slags as well. Enrichment of SiO_2 in the infiltrated slags should increase their viscosity.
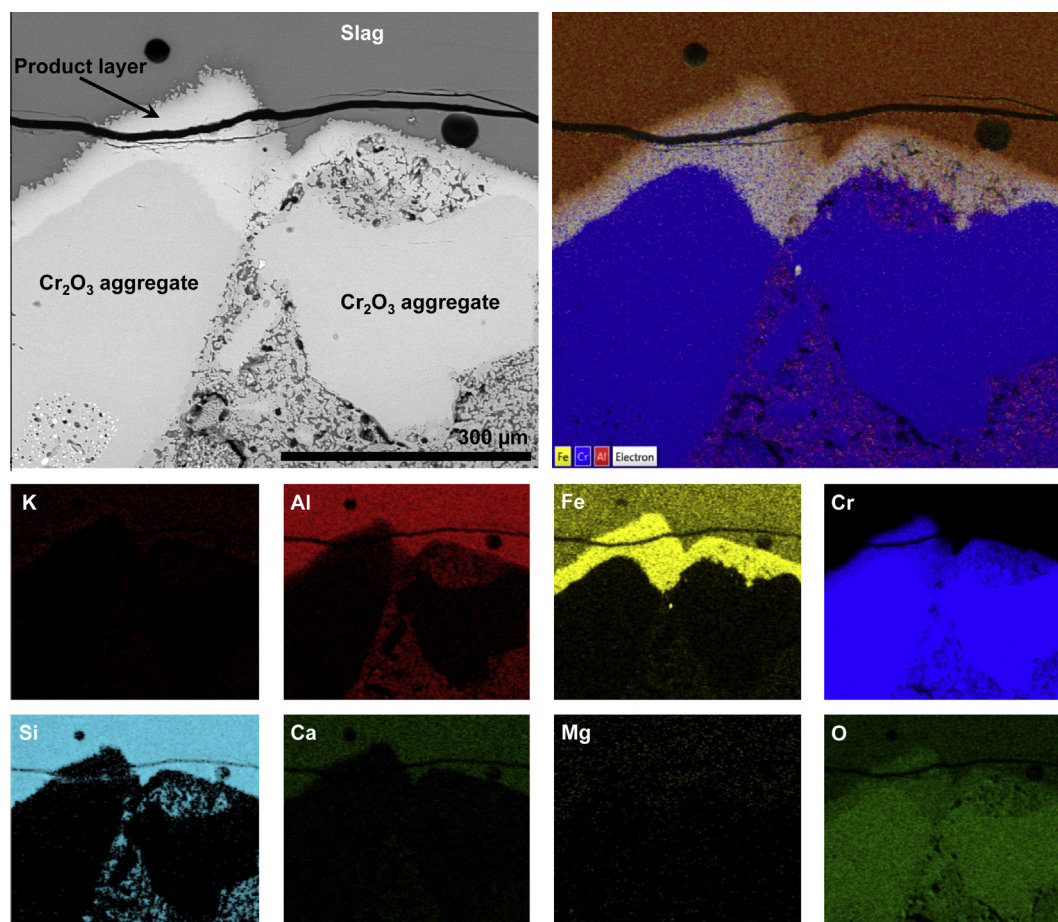

Fig. 9. BSE micrograph of top interface of sample infiltrated with EC slag along with the elemental maps.

5. Discussion

From the observations made in the results section, the following points can be summarized with respect to the infiltrations of the four synthetic slags into the Cr_2O_3–Al_2O_3 refractory system:

- Formation of a substantially thick layer of spinel phases on the top interfaces of the refractory obstructed slag infiltration into the 90%Cr_2O_3–10%Al_2O_3 refractory (Figs. 9–12).
- With EC slag, the product layer was comprised mainly of $FeCr_2O_4$-rich layer, on top of which a thin of $FeAl_2O_4$-rich layer formed (Fig. 9).
- ECP slag resulted in a $Fe(Cr,V,Al)_2O_4$ layer, with partial substitution of Al^{3+} and V^{3+} cations into the Cr^{3+} sites (Fig. 10).
- For WC and WCP slags, the layer was mainly $MgCr_2O_4$, with Mg^{2+} partially substituted by Fe^{2+} cations, due to substantially lower FeO and higher MgO contents in the slags (Figs. 11 and 12). Vanadium species did not participate in the formation process of the product layer.
- The overall thickness of the product layers in the fours cases was: ECP > EC > WC ≈ WCP.
- WC and WCP slags demonstrated noticeable degrees of penetration as compared to the EC and ECP slags. SiO_2, CaO, and Al_2O_3 species selectively penetrated beyond the chromium spinel layer.
- The chromium spinel layer that formed with ECP slag was rough and uneven with significant protrusions into the slag fluid (Fig. 10).

5.1. Thermodynamic calculations

The product spinel layers of liquid-solid reactions at the top interface between the slags and 90%Cr_2O_3–10%Al_2O_3 refractory were known to function as barriers to not only block fluid flow into the bulk refractory, but also reduce corrosion by forcing an indirect dissolution path [7,21] between the slag and the virgin refractory material. The chemistries of the solid solution spinel layers reflected the compositions of major constituents of the starting slags. $Fe(Cr,Al)_2O_4$ and $Fe(Cr,Al,V)_2O_4$ formed when refractory were respectively infiltrated with EC and ECP slags, which contained increased concentrations of FeO. $(Mg,Fe)Cr_2O_4$ formed when samples were infiltrated with WC and WCP slags, which contain considerable concentrations of both MgO and FeO.

Pseudo-binary phase diagrams, which simulated the synthetic slags in contact with the refractory, agreed with the experimental infiltration results. Diffusion paths for multi-component systems that contain species with varying diffusivities rarely exhibit direct trajectories in the respective phase fields. The diagrams generated using FactSage v6.3 [22] in Fig. 15 are thus simplifications to represent some of the phases that may appear, assuming that the species behave similarly to one another with regard to diffusion. With the starting slag composition on the left and the refractory compositions on the right, the diagrams qualitatively depict the phases that would appear if the system from the center of the pore to the pore wall were to be viewed as a diffusion couple. The pore wall was assumed to be in local equilibrium with the infiltrating slag. The calculations consider mullite, corundum, spinel,
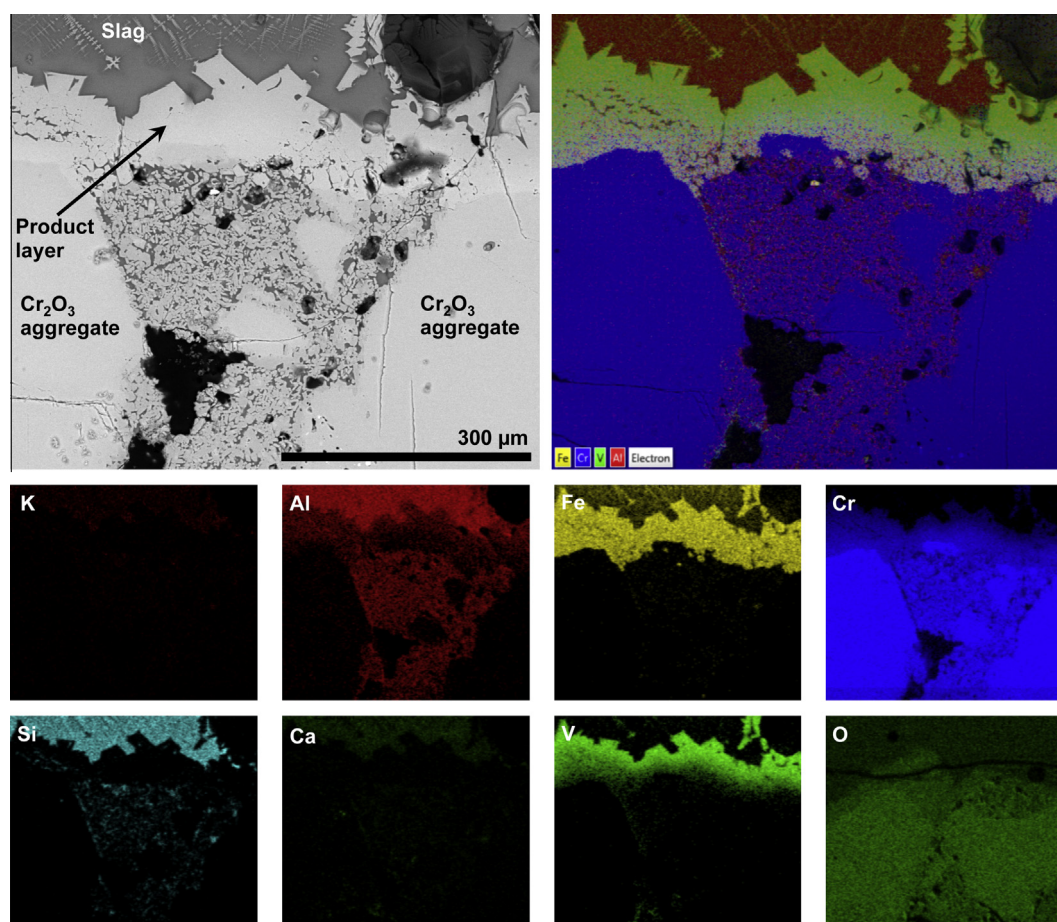

Fig. 10. BSE micrograph of top interface of sample infiltrated with ECP slag along with the elemental maps.
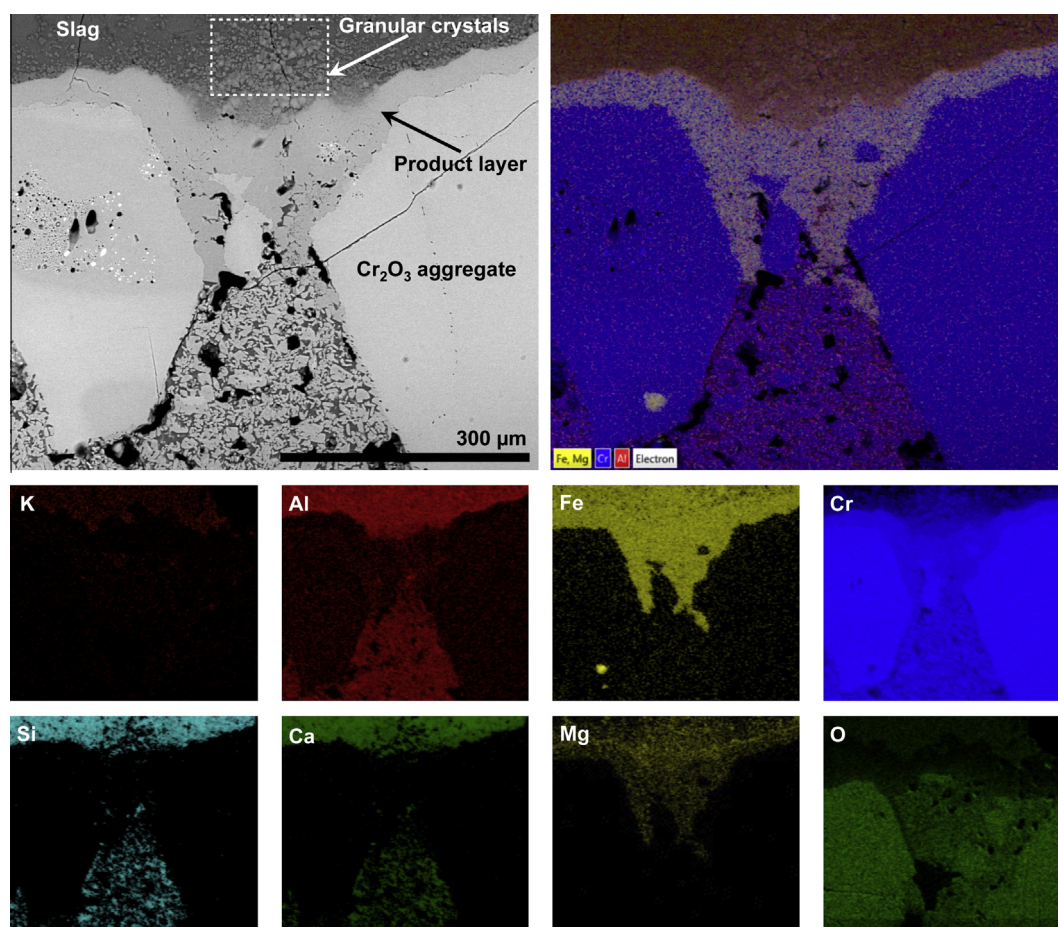
Fig. 11. BSE micrograph of top interface of sample infiltrated with WC slag along with the elemental maps.

aluminate, silicate solution structures and slag as possible phases that could form in the system. To represent the synthetic slag, the Slag A solution phase database was selected since it is optimized for many of the major oxide components in the slag. For both cases and within the relevant temperature range, Fig. 15 shows slag, refractory, and spinel phases in equilibrium with one another. At lower temperatures, melilite, in the form of akermanite, was predicted to form with WC slag. XRD powder scans associated with the WC slag systems in Figs. 3 and 14 both confirm the formation of akermanite. Although equilibrium predictions were also calculated for systems containing ECP and WCP slags, the resulting pseudo phase diagrams were of little use because FactSage lacks the databases to consider vanadium-oxide in solution.

The valence states of V strongly depend on the oxygen partial pressure [7] as shown by the stability diagram of V–O_2 system (Fig. 16) calculated with FactSage v6.3 using database for pure substances. It shows that under the experimental P_{O_2} approximately at 10^{-8} atm, the most stable phase is solid V_2O_3, with a melting point of 2243 K. Although assuming that V-oxides behaved similarly in solution as it did in its pure state was a vast simplification, the V-oxide from the starting slags formed solid solution spinel phases with other cations, such as Fe^{2+}, Mg^{2+} and Al^{3+}, instead of precipitating in the molten slag as V_2O_3 solids alone. This stabilized V as a solid and reduced its activity as a constituent in the slag. This possible mechanism was evident in the XRD scans of the starting EC and ECP slags in Fig. 3. FeV_2O_4 spinel has very high melting point, i.e. 2023 K [23], hence V-rich spinel phases likely remained as solids after ECP slag was melted in refractory cup at 1723 K and later integrated into the product layer.

5.2. The formation of the product layers

As seen in Figs. 9–12, solid–solution spinel product layers formed on the top interface of the refractory, but there are some noticeable morphology, thickness and elemental distribution differences among the product layers with respect to slag chemistries. Before the discussion of the individual characters of the product layers in each case, a generalized description of the processes of the formation of spinel in the context of liquid–solid reaction is as follows [24]:

Taking $FeCr_2O_4$ as an example, upon contact between the molten slag and the surface of solid refractory (large Cr_2O_3 aggregates in particular), small spinel crystals with near stoichiometry nucleated relatively easily. Once the initial spinel layer formed, subsequent growth and thickening of the product layer then depend on two transport processes, i.e. liquid-phase transport of FeO to the slag/$FeCr_2O_4$ interface and solid-state counter-current diffusion process of the reactants, i.e. Fe^{2+} and Cr^{3+}, through the spinel layer, schematically shown in Fig. 17. In the working temperature range of the refractory hot-face (1723 K (1450 °C) and above) and given the content of the FeO in the slag being 15.19% in oxide mol% (as in EC and ECP slags), liquid-phase transport of FeO would be expected to be much faster than solid-state diffusion. Therefore, the solid-state diffusion should be rate-limiting in the thickening of the spinel layer, in which Fe^{2+} cations diffuse away from and Cr^{3+} diffuse toward the slag/$FeCr_2O_4$ interface and vice versa from the $FeCr_2O_4$/Cr_2O_3 interface. During the reaction, in order to maintain electroneutrality at the two reaction fronts and throughout the product spinel, every three Fe^{2+} cations that diffuse to the $FeCr_2O_4$/
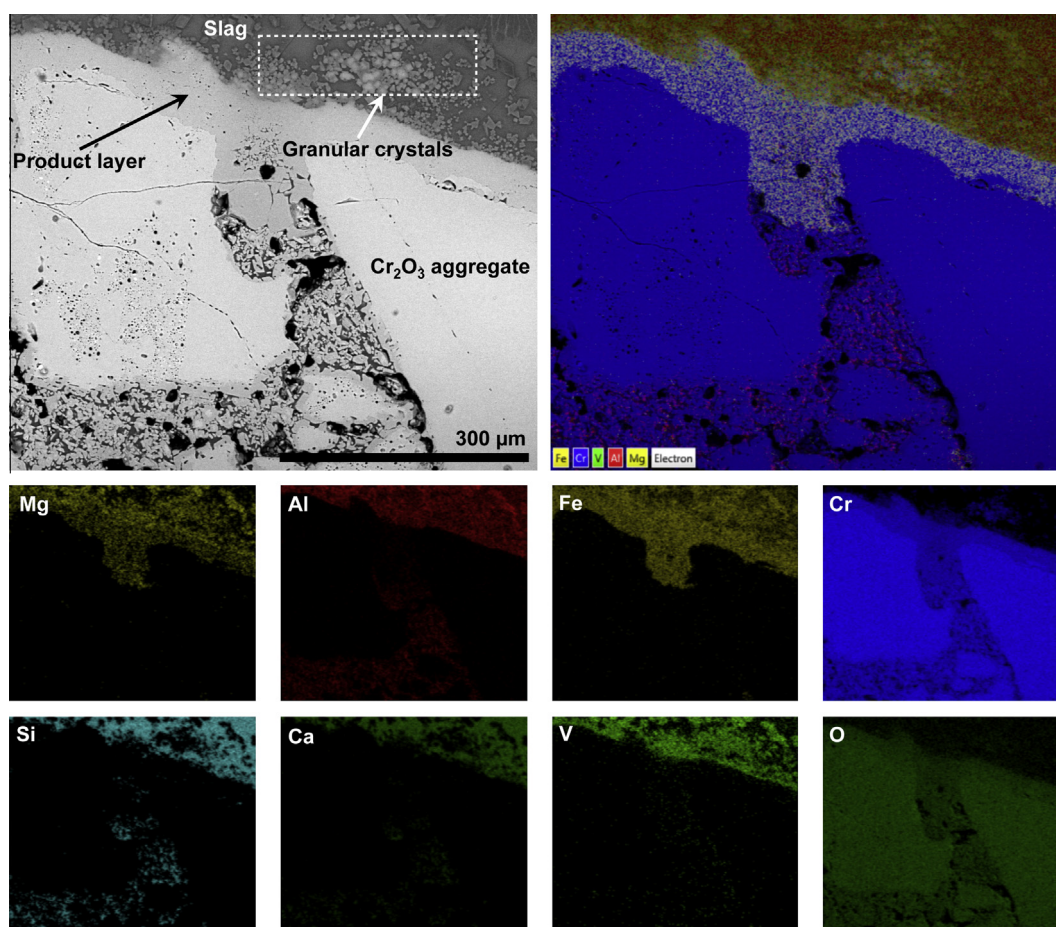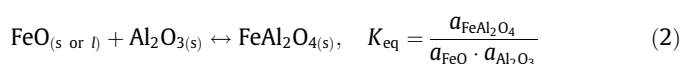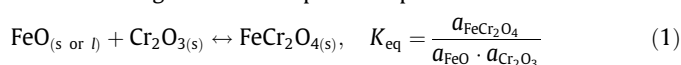
Fig. 12. BSE micrograph of top interface of sample infiltrated with WCP slag along with the elemental maps.

Cr_2O_3 interface are accompanied by two Cr^{3+} cations that diffuse in the opposite direction to the slag/$FeCr_2O_4$ interface. The ideal reactions that occur at the two interfaces are shown in Fig. 17, from which it can be found that the $FeCr_2O_4$/Cr_2O_3 interface should move three times as quickly as the slag/$FeCr_2O_4$ interface [24]. Because the thickening of the spinel is limited by solid-state ionic diffusion, the rate at which the spinel layer thickens should be parabolic as a function of time [25], and the growth rate is particularly low due to the generally low diffusivity of the cations in spinel.

5.3. EC slag

On the sample infiltrated with EC slag, it was seen that the product phase was comprised of two regions with different elemental distributions (Fig. 9), and the phases in the slag/refractory boundary area were in the sequence of slag-$FeAl_2O_4$ (hercynite)–$FeCr_2O_4$(chromite)–Cr_2O_3 refractory aggregate.

The Gibbs free energy ($\Delta G°$) for the formation of chromite and hercynite were calculated using FactSage v6.3 [22], and the results are shown in Fig. 18. The calculations were based on the following reactions using database for pure compounds:

$$FeO_{(s\ or\ l)} + Cr_2O_{3(s)} \leftrightarrow FeCr_2O_{4(s)}, \quad K_{eq} = \frac{a_{FeCr_2O_4}}{a_{FeO} \cdot a_{Cr_2O_3}} \quad (1)$$

$$FeO_{(s\ or\ l)} + Al_2O_{3(s)} \leftrightarrow FeAl_2O_{4(s)}, \quad K_{eq} = \frac{a_{FeAl_2O_4}}{a_{FeO} \cdot a_{Al_2O_3}} \quad (2)$$

The $\Delta G°$ for chromite and hercynite at 1723 K (1450 °C) is −41.89 and −14.87 kJ/mol, with corresponding equilibrium con-

stants (K_{eq}) of 18.61 and 2.82, respectively. Although much simplified, the big difference in the Gibbs free energies of formation and equilibrium constants of the two reactions showed that the formation of $FeCr_2O_4$ should be much favored thermodynamically over $FeAl_2O_4$.

It was therefore hypothesized that the $FeCr_2O_4$ product layer formed by the reaction between Fe species in the melt and Cr species in the solid refractory, and thickened by counter-current diffusion of Fe cations into the Cr_2O_3 aggregate and Cr cations toward the slag. At 1723 K (1450 °C), the diffusion coefficient of Fe^{2+} in $FeCr_2O_4$ was two orders of magnitudes higher than Cr^{3+}, on the order of 10^{-9} cm^2 s^{-1}, extrapolated from ref [26]. At low oxygen activity, the dominant point defects of spinels were observed to be interstitial ions and electrons [27]. As describe earlier, the $FeCr_2O_4$/Cr_2O_3 interface moved much faster than the slag/$FeCr_2O_4$ interface, which was supported by the fact that the $FeCr_2O_4$/Cr_2O_3 interface seemed quite smooth.

With the predominant inward growth of the $FeCr_2O_4$ layer, small amount of Al^{3+} also solutioned into the spinel during the process. After some time, the growth rate of the $FeCr_2O_4$ layer slowed down as the diffusion of both Fe and Cr cations across the product layer gradually became the rate-limiting step such that Fe species accumulated at the slag/$FeCr_2O_4$ interface. With no excess Cr^{3+} but abundant Al^{3+} from the slag in the vicinity, hercynite nucleated on the chromite surface. Because of the similarities in the crystal structure and lattice parameters, the energy barrier for such nucleation should be relatively small. It should also be noted that hercynite most likely grew into the liquid as made evident by its faceted and rough surface.
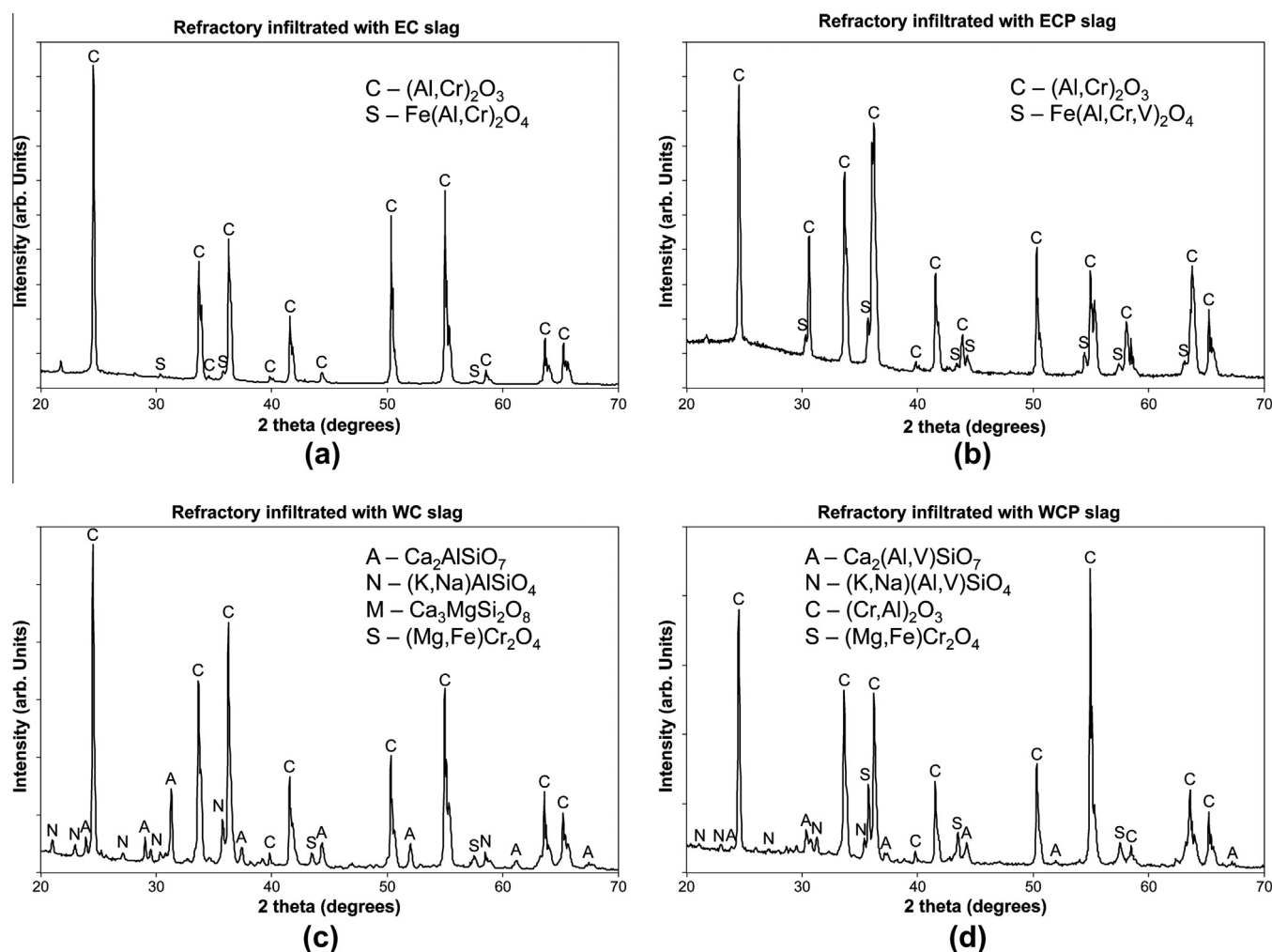
Fig. 13. XRD powder scans of refractory samples infiltrated with (a) EC, (b) ECP, (c) WC, and (d) WCP slags.

5.4. ECP slag

The formation of the product layer from ECP slag should be somewhat similar to the hypothesized process in the case of EC slag: the chromite mainly grew with inward diffusion of Fe cations into the Cr_2O_3 aggregate while solutioning small amounts of Al and V species. Meanwhile, either the existing V-rich spinel from the starting slags integrated into the chromite layer or new V-rich spinel nucleated on the chromite surface and grew into the liquid slag, forming a very faceted and jagged surface. Slightly different from the case with EC slag, solid-state counter-current diffusion of Cr and V species seemed to have also occurred in the product layer and finally resulted in the concentration gradients shown in Fig. 14. The incorporation of V-rich spinel also significantly increased the thickness of the product layer.

Comparing the cases of EC and ECP slags, while both Al_2O_3 and V_2O_3 can react with FeO to form spinels either in the melt or by liquid–solid reaction, $FeAl_2O_4$ formed in much smaller quantities in EC than V-rich spinel in ECP, and the contribution from $FeAl_2O_4$ to the product layer was much less than that from V-rich spinel. On one hand, in terms of the formation of V-spinel, assuming the simplified reaction to be the following without considering its non-stoichiometry:

$$FeO_{(s\ or\ l)} + V_2O_{3(s)} \leftrightarrow FeV_2O_{4(s)}, \quad K_{eq} = \frac{a_{FeV_2O_4}}{a_{FeO} \cdot a_{V_2O_3}} \quad (3)$$
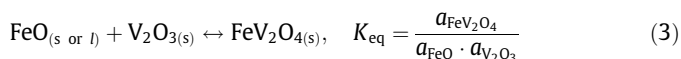
The $\Delta G°$ and K_{eq} for V-spinel at 1723 K (1450 °C) are −18.89 kJ/mol and 3.74, respectively, comparing to −14.87 kJ/mol and 2.82 of

hercynite, also see Fig. 18. It can hence be inferred that FeV_2O_4 is also thermodynamically favored than $FeAl_2O_4$ under the condition in this study. On the other hand, in terms of forming solid-solution with $FeCr_2O_4$, the solutioning between FeV_2O_4 and $FeCr_2O_4$ must be significantly favored energetically than that between $FeAl_2O_4$ and $FeCr_2O_4$. Due to the lack of data concerning V in solution, this cannot be validated by thermodynamic calculation. Nevertheless, these may be the reasons why the product layer resulted from ECP slag was much thicker than that from EC slag.

5.5. WC and WCP slags

For WC and WCP slags, the product layer was mainly $MgCr_2O_4$, with Mg^{2+} partially substituted by Fe^{2+} cations, (Figs. 11 and 12). The formation of $MgCr_2O_4$ and $FeCr_2O_4$ are both thermodynamically favored over aluminous spinels, Fig. 18, and the MgO content in the melt was higher than FeO content, $MgCr_2O_4$ thus became the base product and Fe^{2+} substituted approximately one third of the Mg^{2+} sites.

When the Cr_2O_3–Al_2O_3 refractory interacted with ECP slag, V^{3+} cations substituted into approximately 30% of the Cr^{3+} sites of the spinel structure. An analogous substitution of V^{3+} cations did not occur for when the Cr_2O_3–Al_2O_3 refractory interacted with WCP slag. The integrated product layer solely consisted of $(Mg,Fe)Cr_2O_4$. V_2O_3 instead formed $(Mg,Fe)(Cr,Al,V)_2O_4$ solid solution crystals that were suspended above the integrated product layer.
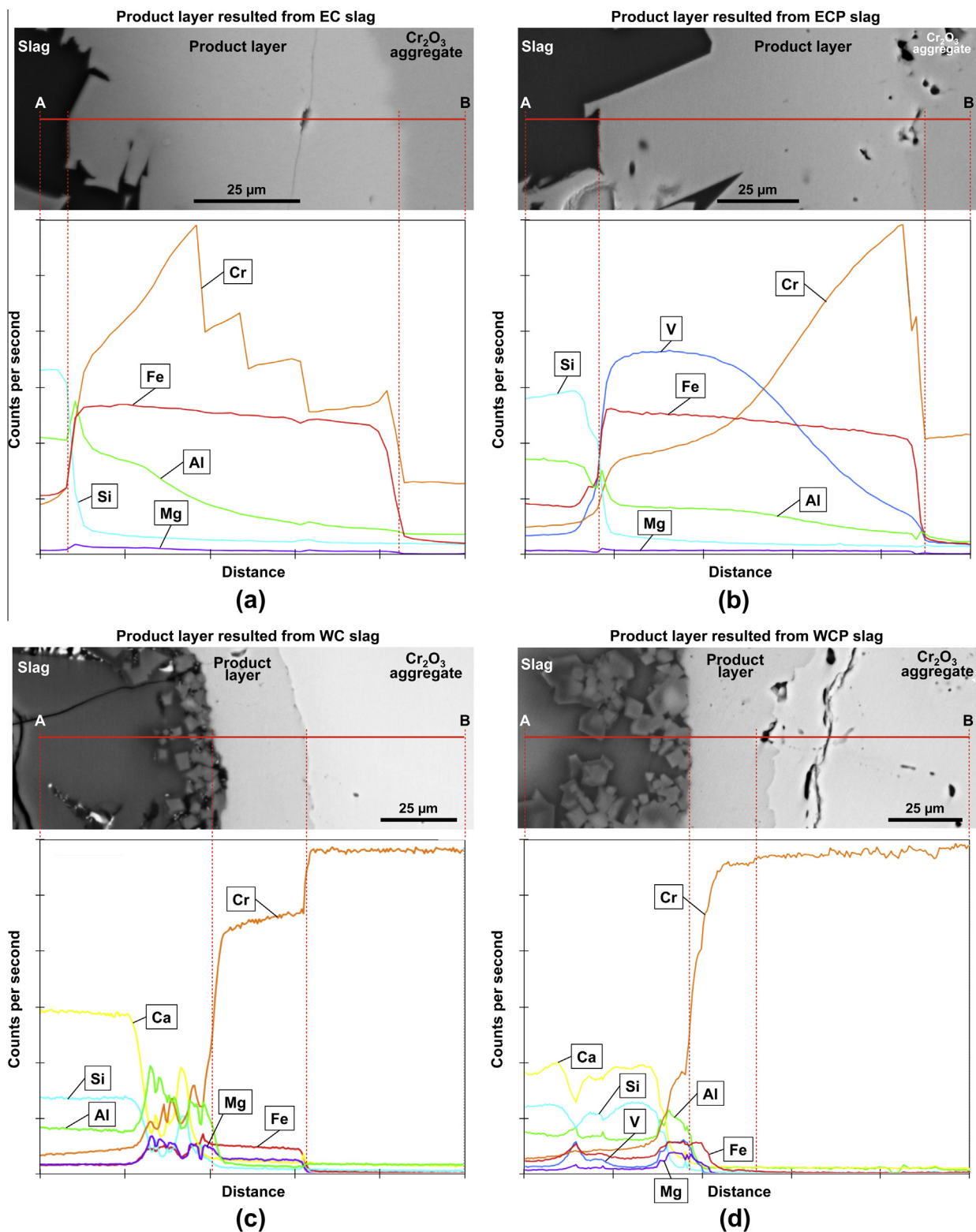
Fig. 14. BSE micrograph of top interface of sample infiltrated with (a) EC, (b) ECP, (c) WC and (d) WCP slags accompanied by EDS elemental profiles along lines labeled as AB.

One possibility that the V^{3+} substitution into the Cr^{3+} sites occurred with ECP slag but not with WCP slag was that the free energy of mixing for the substitution of V^{3+} into Cr^{3+} sites possibly increased when the base spinel phase changed from $FeCr_2O_4$ to $MgCr_2O_4$. In other words, the majority 2+ cations changed from Fe^{2+} to Mg^{2+}. Equally, simultaneous solutioning of Al^{3+} into Cr^{3+} site

in the case of ECP slag may have lowered the free energy of mixing for the substitution of V^{3+} into Cr^{3+} sites even though Mg^{2+} has substituted a fraction of Fe^{2+} sites in the base spinel phase.

Assuming the suspended crystals formed during infiltration experiment, whether they were in the process of detaching from or appending onto the integrated layer was unclear. Nevertheless,

Table 4
Average compositions of slags that infiltrated into the refractory. Results are presented in oxide mol%.

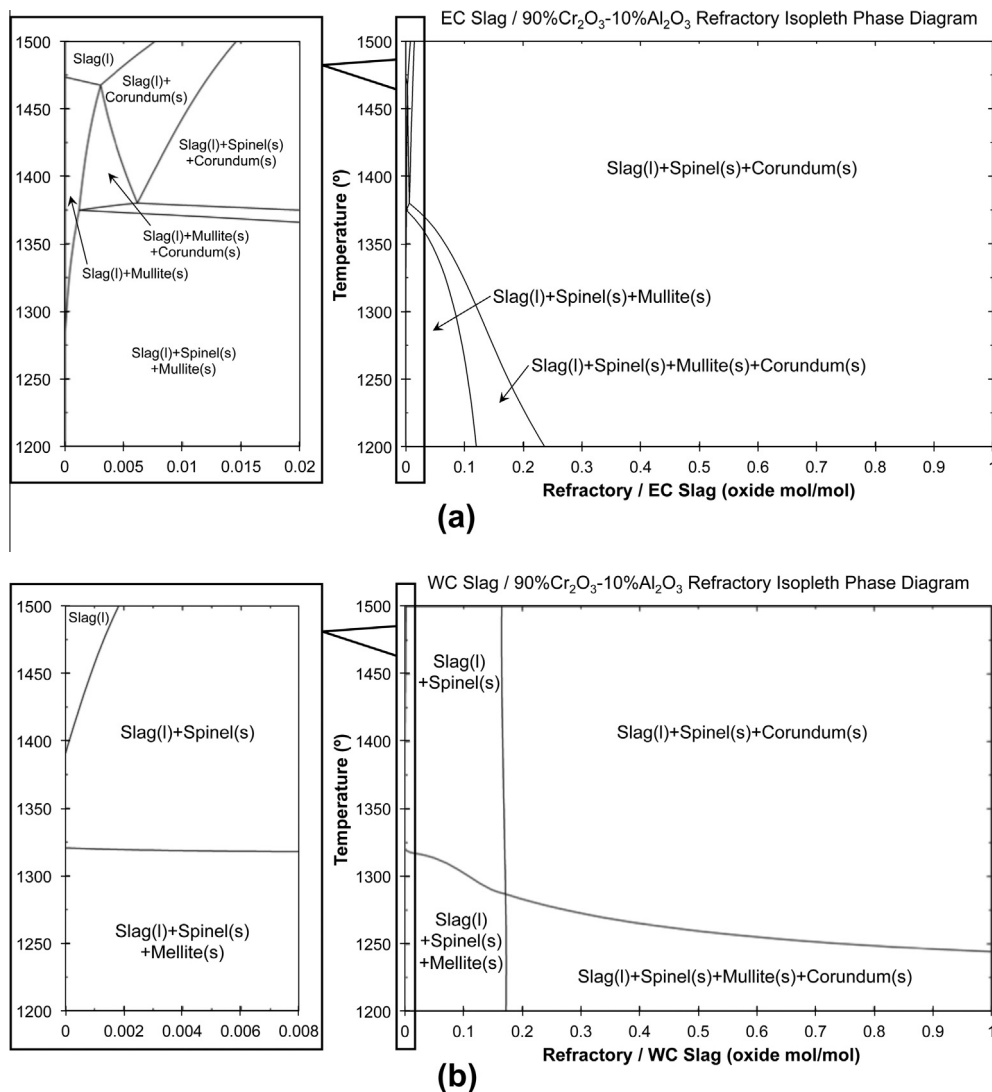| Infiltrating slags	Al_2O_3 (%)	SiO_2 (%)	FeO (%)	CaO (%)	MgO (%)	Na_2O (%)	K_2O (%)	V_2O_3 (%)
EC	26.9	54.4	7.7	6.7	0.7	1.1	2.4	0
ECP	14.7	66.0	7.2	7.4	1.1	1.1	1.6	0.9
WC	14.2	44.0	1.3	33.2	3.2	3.9	2.6	0
WCP	13.2	44.7	1.1	31.9	2.8	3.2	2.3	0.4

Fig. 15. Pseudo-binary phase diagrams, which simulate 90%Cr_2O_3–10%Al_2O_3 refractory in contact with (a) EC and (b) WC slags.

two possibilities may account for these granular crystals. (a) The matrix region in the refractory contains small chromia and alumina particles and the alumino-silicate bonding systems, which held the much bigger chromia and alumina aggregates together. It was possible that the alumino-silicate bonding systems in the matrix region were aggressively attacked by WC and WCP slags that were much more basic than EC and ECP slags. Similar attacks on the bonding systems of alumina crucible by basic slags were seen in earlier studies [28,29]. As a result, the small particles of alumina and chromia in the matrix regions were released from the refractory and entered the slag, which consequently reacted with the Fe^{2+}, Mg^{2+} cations and V species in the slag and formed the granular crystals seen suspended in the slag in the vicinity of the product layer. (b) Due to higher basicity of the WC and WCP slags, chemical dissolution of Cr_2O_3 refractory material by the slag might be substantial and hence these granular crystals could be the reaction product between the dissolved Cr_2O_3 and the spinel-forming species in the slag, and they were in the process of appending onto the integrated product layer.

With little participation of Al and V cations in the formation of the integrated product layer in WC and WCP slags, the thickness of the product layer would depend on the concentration of 2+ cations in the slag. If it was true that the integrated product layer grew mainly by inward diffusion of Mg and Fe cations, given the same starting contents of combined MgO and FeO in the slags, the thickness of the product layers should be somewhat similar within the same amount of time. This was supported by the experimental observation that the thickness of the product layers from the WC
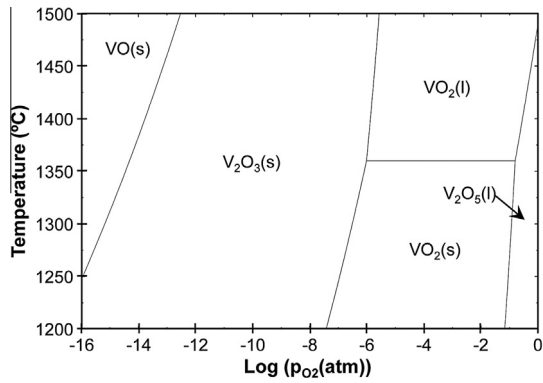
Fig. 16. Temperature vs. P_{O_2} stability diagram for vanadium. Within experimental parameters, solid V_2O_3 is most stable.
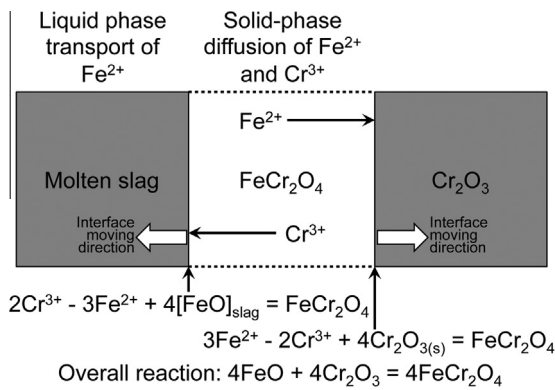

Fig. 17. Schematic drawing of the formation process of the $FeCr_2O_4$ spinel product layer.

and WCP slags was similar within experimental errors, and the combined MgO and FeO contents in these two slags were 19.95% and 16.97% (oxide mol% normalized without V), respectively. In

the case of ECP slag, vanadium evidently participated in the product layer formation, therefore, although FeO + MgO contents in EC and ECP slags was about the same, ECP slag produced a much thicker product layer.

It was also suspected that the higher basicity (CaO/SiO$_2 \approx 1.0$) of the WC and WCP slags affected the formation of the spinel product layer in some indirect way. Albertsson et al. found that the activity of Cr_2O_3 in the liquid phase was seen increased with basicity (1.0–1.4) [30]. It was also known that, in the quaternary system of CaO–FeO–MgO–SiO$_2$, the activity of FeO increased with increasing (CaO + MgO)/SiO$_2$ ratio in the range of 0–0.2, but then quickly decreased with the ratio greater than 0.2 [31,32].

On the other hand, the suspended spinel crystals containing Al_2O_3 and V_2O_3 suggested that the interaction between the slag and the refractory had not reached equilibrium at 5 h. In the practical gasification process, the residence time of slag in the gasifier chamber has been estimated to be on the order of ~30 min [29], hence equilibrium in fact cannot be achieved. Also, the continuous flow of slag along the hot-face of the refractory wall would most likely flush the suspended spinel crystals downstream such that they could not integrate into the product layer. Therefore, additional shorter infiltration times need to be studied so as to determine the direction of the reaction kinetics and the corresponding slag infiltration behavior.

Moreover, although the product layers that formed on the top interfaces of the samples prevented excessive slag infiltration into the refractory, their effectiveness needs to be evaluated in actual gasification conditions where fresh incoming slag continuously flows along the refractory walls. As shown in Fig. 10, the $Fe(Cr,Al,V)_2O_4$ layer formed jagged facets that protruded into the slag fluid. The uneven morphology of the layer can pose operational problems since the additional surfaces of the protruded grains can increase any tangential force associated with the flow of the slag. The sharp corners of the grains can induce vorticities, and further increase the tangential forces. The protective $Fe(Cr,Al,V)_2O_4$ layer can cause higher spallation rates as a result of the increased forces associated with its unique morphology. Studies that consider relative velocities between the slag and the refractory are needed to further examine this possible spallation
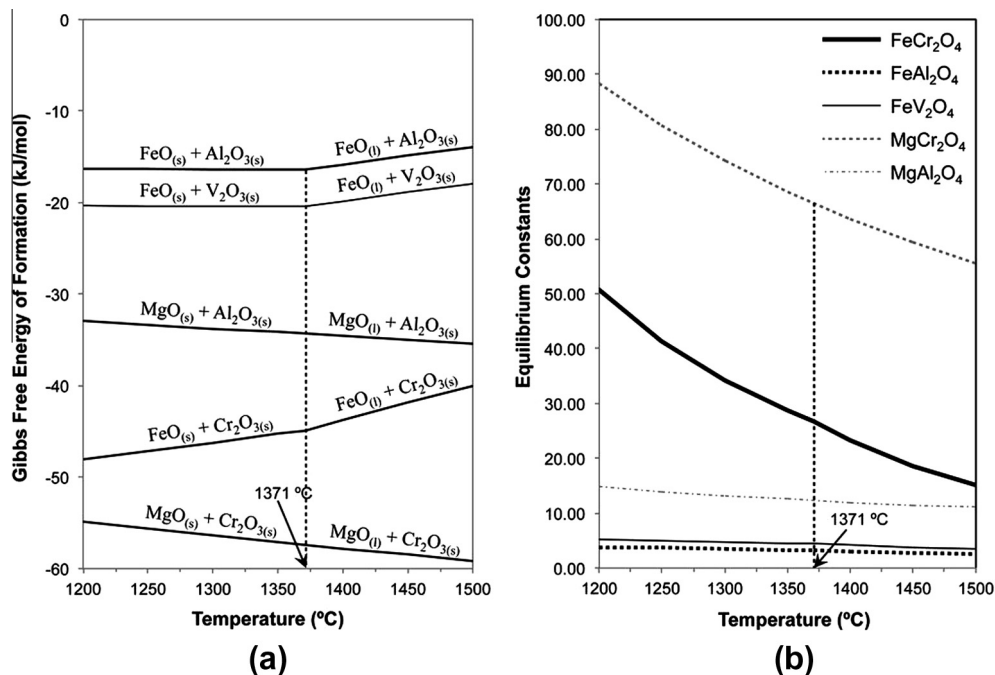

Fig. 18. The Gibbs free energy of formation for spinel phases and the corresponding equilibrium constants.

Table 5
Thermal expansion coefficients of refractory material and product spinels.

Materials	Thermal expansion coefficients mm/mm/K (mm/mm/°C)	Refs.
Cr_2O_3–Al_2O_3 refractory (hot-face)	8.2×10^{-6}	[7]
$FeCr_2O_4$	8.5×10^{-6}	[33]
$MgCr_2O_4$	9.3×10^{-6}	
$FeAl_2O_4$	9.0×10^{-6}	
$MgAl_2O_4$	8.1×10^{-6}	

mechanism. Also, thicker product layers with mismatch in thermal expansion coefficients, if significant enough, were in general more likely to spall. Table 5 lists the thermal expansion coefficients of the refractory and product spinels. Small cracks and voids at the interface between the product layer and the refractory were seen in the present study in the cases of ECP, WC and WCP slags.

5.6. Infiltration of the slag into the porous refractory

Thick layers of chromium spinel resulted from the liquid-solid reactions at the top interface between the slags and 90%Cr_2O_3–10%Al_2O_3 refractory functioned as barriers to block excessive fluid flow into the bulk refractory and to limit the slag infiltration into the refractory microstructure. The refractory corrosion was hence forced into an indirect dissolution path [7,21] between the slag and the virgin refractory material. The formation of chromium spinel also highly modified the composition of the slag that infiltrated beyond the barrier layer.

Nevertheless, all four slags penetrated beyond the protective product layers as shown both macroscopically (Fig. 8) and microscopically (Figs. 9–12). The extent of these limited infiltrations can be attributable to a few distinct scenarios. The first possibility is that the chromium spinel product layer did not fully seal the refractory from the slag, and thus allowed volumes of slag to slowly infiltrate into the porous matrix regions. During this process, reactions between the slags and the refractory depleted the slag of its FeO and MgO content, which led to enrichment in SiO_2, CaO, and Al_2O_3 species. The second possibility is that the product layer successfully blocked fluid flow, but the ionic species of Si^{4+}, Ca^{2+}, and Al^{3+} preferentially passed through the layer by means of ionic diffusion. At low oxygen partial pressures, spinel structures are known to consist of cation interstitials [34], which typically diffuse at greater rates than cation vacancies. The third possibility is that volumes of slag infiltrated into the refractory before a fully integrated layer was able to protect the refractory. The extent of infiltration would be dictated by a competition of rates between the growth of chromium spinel and the penetration of slag driven by capillarity pressures. The temperature and the diffusivity of the species in the liquid slag is regarded as the limiting term for infiltration, while the corresponding solid-state ionic diffusivity of the species determine the growth rate of the product layer.

Diffusivities of cations in oxide melts decrease with increasing ionic radii and atomic number, and also with increasing slag polymerization, as indirectly indicated by viscosity [7,12]. In partly polymeric melts, the diffusivity of an ion is governed by its mobility, while the viscosity of the fluid is determined by the network-forming species [12]. If the microstructure is considered as a system of highly interconnected pores, slag infiltration with respect to time can be projected by assuming fluid flow through capillary channels. Since the characteristic length scale of a pore in the radial direction is significantly shorter than in the penetration direction, a lubrication approximation was applied to simplify the momentum equation to Eq. (4) [35].

$$\bar{u}_z = \frac{dl}{dt} = \frac{R\gamma \cos\theta}{4 \int_0^{l(t)} \eta(z)dz} \tag{4}$$

where R is the pore radius, γ is the surface tension of the slag, θ is the contact angle of the slag with the pore wall, η is the dynamic viscosity of the slag, and l is the penetration depth of the slag that is perpendicular to the slag/refractory interface. Fig. 4 shows that the viscosity of the slag strongly dictates the rate of slag infiltration. Given that the size of the Fe^{2+} cation is larger than that of the Mg^{2+} cation, the $(Mg,Fe)Cr_2O_4$ layer that formed with WC and WCP slags grew at lower rates as compared to the $FeCr_2O_4$-rich layer that formed with EC and ECP slags. The lower viscosities of the WC and WCP slags allowed for WC slag systems to infiltrate more quickly than the EC slag systems. Consequently, WC and WCP slags penetrated into the refractory until an integrated product layer, capable of blocking fluid flow, fully formed. Although penetrations were on the order of millimeters, the infiltrated slag with increased concentrations of SiO_2, CaO and Al_2O_3 can gradually solution with the glassy alumino-silicate bonding phase of the refractory and degrade the mechanical and thermal properties of the refractory microstructure. The protective product layer can ultimately spall away due to weakening of the underlying refractory substrate. Examination of additional infiltration times will help determine which of mentioned mechanisms is most dominant.

6. Conclusion

Synthetic slags with compositions resembling the mineral impurity constitution of potential gasification feedstock were infiltrated into 90%Cr_2O_3–10%Al_2O_3 refractory to investigate the effects of slag composition on the infiltration characteristics of the slags. Regardless of feedstock variation, interactions between the refractory and the slags uniformly produced layers of chromium spinel on the top interfaces of the samples. The solid solution chemistries of the chromium spinel varied depending on the composition of the infiltrating slag. $Fe(Cr,Al)_2O_4$ formed when refractory interacted with eastern coal (EC) slag, which contains high concentrations of FeO. $(Mg,Fe)Cr_2O_4$ formed when refractory came in contact with western coal (WC), which contains comparable concentrations of both MgO and FeO. The eastern coal - petcoke (ECP) formed similar solid phases as its EC slag counterpart, but with additions of V_2O_3 in the solid solution chemistries. Vanadium species did not integrated into the product layer in the western coal–petcoke (WCP) slag infiltration experiment. The $Fe(Cr,V,Al)_2O_4$ layer that formed with the ECP slag demonstrated an uneven morphology, which can cause increased spallation rates in actual gasification conditions. The viscosity of the 4 study slags was measured in the temperature range of 1773–1573 K (1500–1300 °C). The viscosity of WC and WCP slags was much lower than EC and ECP slags. The viscosity differences between the slags strongly dictated the penetration depth. As compared to EC and ECP slags, WC and WCP slags penetrated beyond the protective product layers and deeper into the refractory. Although the chromium spinel layers limited infiltration by effectively blocking the slag from flowing into the porous microstructure of the refractory, the viability of the mechanism requires further investigation using methodologies that can simulate relative velocities between the slag and refractory materials.

Disclaimer

"This report was prepared as an account of work sponsored by an agency of the United States Government. Neither the United States Government nor any agency thereof, nor any of their employees, makes any warranty, express or implied, or assumes

any legal liability or responsibility for the accuracy, completeness, or usefulness of any information, apparatus, product, or process disclosed, or represents that its use would not infringe privately owned rights. Reference herein to any specific commercial product, process, or service by trade name, trademark, manufacturer, or otherwise does not necessarily constitute or imply its endorsement, recommendation, or favoring by the United States Government or any agency thereof. The views and opinions of authors expressed herein do not necessarily state or reflect those of the United States Government or any agency thereof."

Acknowledgements

References

[1] Bennett JP, Kwong KS, Dogan CP, Chinn RE. Improved refractory for slagging gasifiers in IGCC power systems. In: 18th Annual conference on fossil energy materials. oak ridge national laboratory, fossil energy program. Oak Ridge, TN: Knoxville, TN; 2004.

[2] Lee WE, Zhang S. Melt corrosion of oxide and oxide-carbon refractories. Int Mater Rev 1999;44(3):77–104.

[3] Brosnan DA. Corrosion of refractories. In: Schacht CA, editor. Refractories handbook. New York: Marcel Dekker; 2004. p. 39–77.

[4] Blond E, Schmitt N, Hild F, Blumenfeld P, Poirier J. Effect of slag impregnation on thermal degradations in refractories. J Am Ceram Soc 2007;90(1):154–62.

[5] <http://www.netl.doe.gov/technologies/coalpower/gasification/worlddatabase/index.html>.

[6] Bennett JP, Kwong KS. Improved refractories for slagging gasifiers in IGCC power systems. <http://www.osti.gov/bridge/purl.cover.jsp?purl=/899004-9XxkMf/899004.pdf>.

[7] Bennett JP, Kwong KS. Failure mechanisms in high chrome oxide gasifier refractories. Metall Mater Trans A 2011;42A:888–904.

[8] Nakano J, Kwong KS, Bennett JP, Lam T, Fernandez LM, Komolwit P, et al. Phase equilibria in synthetic coal–petcoke slags (Al_2O_3–CaO–FeO–SiO_2–V_2O_3) under simulated gasification conditions. Energy Fuels 2011;25:3298–306.

[9] Greenberg S, Poeppel RB. The corrosion of ceramic refractories exposed to a synthetic coal slag by means of the rotating-drum technique. Research report no. ANL/FE-85-9. Argonne, IL: Argonne National Laboratory. p. 1–15.

[10] Greenberg S, Poeppel RB. The corrosion of ceramic refractories exposed to synthetic coal slags by means of the rotation-cylinder technique: final report. Research report no. ANL/FE-85-15. Argonne, IL: Argonne National Laboratory; April 1986. p. 1–66.

[11] Kennedy CR, Poeppel RB. Corrosion resistance of refractories exposed to molten acidic coal-ash slags. Interceram 1978;27(3):221–6.

[12] Kennedy CR, Swaroop R, Jones DJ, Fousek RJ, Poeppel RB, Stahl D. Evaluation of ceramic refractories for slagging gasifiers: summary of progress to date. ANL report no. 78-61. Argonne, IL: Argonne National Laboratory; September 1978.

[13] Starzacher AP. Picrochromite brick – a qualified material for texaco slagging gasifiers. Radex-Rundschau 1988;1:491–501.

[14] Bakker WT, Greenberg S, Trondt M, Gerhardus U. Refractory practice in slagging gasifiers. Am Ceram Soc Bull 1984;63(7):870–6.

[15] Guo Z. Refractories for gasifiers. Am Ceram Soc Bull; June 2004. <www.ceramicbulletin.org>.

[16] Selvig WA, Gibson FH. Analyses of ash from United States coals. Volume 567 of bulletin (United States Bureau of Mines). United States Government Printing Office: Washinton, DC; 1956.

[17] Mills KC. Viscosities of molten slags. In: Eisenhuttenleute VD, editor. Slag atlas. Sawston, Cambridge, UK: Woodhead Publishing Limited; 1995. p. 351.

[18] Seetharaman S, Mukai K, Sichen D. Viscosities of slags – an overview. In: VII international conference on molten slags fluxes and salts. The South African Institute of Mining and Metallurgy: Cape Town, South Africa; 2004.

[19] Kaneko TK, Bennett JP, Sridhar S. Effect of temperature gradient on industrial gasifier coal slag infiltration into alumina refractory. J Am Ceram Soc 2011;94(12):4507–15.

[20] Nakano J, Sridhar S, Bennett JP, Kwong KS, Moss T. Interactions of refractory materials with molent gasifier slags. Int J Hydrogen Energy 2011;36(7):4595–604.

[21] Mccallum N, Barrett LR. Some aspects of the corrosion of refracotries. Trans Br Ceram Soc 1952;51:523–43.

[22] Bale CW, Chartrand P, Decterov SA, Eriksson G, Hack K, Mahfoud RB, et al. FactSage thermochemical software and databases. Calphad 2002;62:189–228.

[23] Liao SM, Bo TL, editors. Vanadium metallurgical abroad, vol. 102. Beijing: Metallurgical Industry Press; 1985.

[24] Zhang S, Lee WE. Spinel-containing refractories. In: Schacht CA, editor. Refractories handbook. New York: Marcel Dekker; 2004. p. 215–57.

[25] Kaur I, Mishin Y, Gust W. Fundamentals of grain and interphase boundary diffusion. third ed. New York: John Wiley & Sons; 1995.

[26] Gilewicz-Wolter J, Zurek Z, Dudala J, Lis J, Homa M, Wolter M. Diffusion rates of 51Cr, 54Mn and 59Fe in $MnCr_2O_4$ and $FeCr_2O_4$ Spinels. Adv Sci Technol 2006;46:27–31.

[27] Lee JH, Martin M, Yoo HI. Self- and impurity cation diffusion in manganese–zinc–ferrite, $Mn_{1-x-y}Zn_xFe_{2+y}O_4$. J Phys Chem Solids 2000;61:1597–605.

[28] Zhu J, Kaneko TK, Mu H, Bennett JP, Sridhar S. Effects of measurement materials and oxygen partial pressure on the viscosity of synthetic eastern and western United States coal slags. Energy Fuels 2012;26:4465–74.

[29] Ilyushechkin AY, Duchesne MA, Hla SS, Macchi A, Anthony EJ. Interaction of vanadium-rich slags with crucible materials during viscosity measurements. J Mater Sci 2013;48:1053–66.

[30] Albertsson Galina Jelkina. Licentiate thesis. Investigations of stabilization of Cr in spinel phase in chromium-containing slags. St Ckholm, Sweden: Royal Institute of Technology; 2011.

[31] Taylor CR, Chipman J. Equilibria of liquid iron and simple basic and acid slags in a roatation induction fuenace. Trans AIME 1943;154:228–47.

[32] Bishop Jr HL, Lander HN, Grant NJ, Chipman J. Equilibria of sulfur and oxygen between liquid iron and open hearth-type slags. J Met 1956;8:862–8.

[33] Parmelee CW, Badger AE, Ballam GA. A study of a group of typical spinels. Bulletin no. 248. University of Illinois Urbana-Champaign, Engineering Experiment Station (June 1932). <https://www.ideals.illinois.edu/bitstream/handle/2142/4420/engineeringexperv00000i00248_ocr.txt?sequence=2>.

[34] Dieckmann R, Schmalzried H. Defects and cation diffusion in magnetite. Berichte der Bunsengesellschaft für physikalische Chemie 1977;81(4):414–9.

[35] Kaneko TK, Zhu J, Thomas H, Bennett JP, Sridhar S. Influence of oxygen partial pressure on sythetic coal slag infiltratin into porous Al_2O_3 refractory. J Am Ceram Soc 2012;95(5):1764–73.